Targeting and in vivo imaging of non-small–cell lung cancer using nebulized multimodal contrast agents

Andrea Bianchi[a], Sandrine Dufort[b,c,d], François Lux[e], Pierre-Yves Fortin[a], Nawal Tassali[a], Olivier Tillement[e], Jean-Luc Coll[c,d], and Yannick Crémillieux[a,1]

[a]Centre de Résonance Magnétique des Systèmes Biologiques, Centre National de la Recherche Scientifique Unité Mixte de Recherche 5536, Université Bordeaux Segalen, 33076 Bordeaux, France; [b]Nano-H SAS, 38070 Saint Quentin–Fallavier, France; [c]Institut National de la Santé et de la Recherche Médicale Unité 823 and [d]Université Joseph Fourier, Institut Albert Bonniot, 38706 Grenoble, France; and [e]Institut Lumière Matière, Unité Mixte de Recherche 5306, Université Lyon 1, Centre National de la Recherche Scientifique, Université de Lyon, 69622 Villeurbanne Cedex, France

Edited by Adriaan Bax, National Institutes of Health, Bethesda, MD, and approved April 14, 2014 (received for review February 7, 2014)

One of the main reasons for the dismal prognosis of lung cancer is related to the late diagnosis of this pathology. In this work, we evaluated the potential of optimized lung MRI techniques and nebulized ultrasmall multimodal gadolinium-based contrast agents [ultrasmall rigid platforms (USRPs)] as a completely noninvasive approach for non-small–cell lung cancer (NSCLC) in vivo detection. A mouse model of NSCLC expressing the luciferase gene was developed. Ultrashort echo-time free-breathing MRI acquisitions were performed before and after i.v. or intrapulmonary administration of the nanoparticles to identify and segment the tumor. After orotracheal or i.v. administration of USRPs, an excellent colocalization of the position the tumor with MRI, bioluminescence and fluorescence reflectance imaging, and histology was observed in all mice. Significantly higher signal enhancements and contrast-to-noise ratios were observed with orotracheal administration using lower doses, reducing the toxicity issues and the interobserver variability in tumor detection. The observations suggested the existence of an unknown original mechanism (different from the enhanced permeability and retention effect) responsible for this phenomenon. MRI and USRPs were shown to be powerful imaging tools able to detect, quantify, and longitudinally monitor the development of submillimetric NSCLCs. The absence of ionizing radiation and high resolution MRI, along with the complete noninvasiveness and good reproducibility of the proposed protocol, make this technique potentially translatable to humans. To our knowledge this is the first time that the advantages of an orotracheal administration route are demonstrated for the investigation of the pathomorphological changes due to NSCLCs.

lung tumor | magnetic resonance imaging | bioluminescence imaging | gadolinium-based nanoparticles

Lung cancer is the leading cause of cancer deaths worldwide and the third cancer for occurrence in both sexes, after breast and prostate (1, 2). The burden of this disease is impressive because it is estimated that lung cancer is responsible for more than 1.3 million deaths per year (1, 2). Among the histological variants of this pathology, the non-small–cell lung cancer (NSCLC) known as adenocarcinoma has been increasing in many countries in the past few decades, becoming the most common type of lung cancer in smokers but also in lifelong nonsmokers (1, 3–5).

Despite the advances in medical treatments and radiation-based therapies (5), the 5-y survival rate for lung cancer is still under 15% (1, 3). One of the main reasons for this discouraging prognosis is related to late diagnosis of this pathology. Indeed, close to 70% of patients with lung cancer present with locally advanced or metastatic disease at the time of diagnosis (3).

In the race to improve global health through early detection of diseases, imaging techniques play a major role because they can provide early diagnostics of pathologies, noninvasive longitudinal patient follow-ups, and help prepare and guide radiotherapy or surgery. MRI has been shown to be especially promising because of high soft tissue contrast, good spatial resolution, and absence of ionizing radiation (6, 7). The latter, in particular, represents a strong advantage over nuclear medicine imaging techniques and computed tomography because it enables repeated acquisitions in patients and screening in old and young patients, without introducing a consistent risk of developing radiation-induced secondary pathologies (8).

MRI was proven to be the most adequate imaging technique for the screening and diagnostics of a number of pathologies in brain, heart, or liver (9). Nevertheless, this consideration cannot yet be applied to the lung, which remains one of the most difficult organs to image with MRI because of its intrinsic properties (motion artifacts, low proton density, numerous susceptibility gradients) (6, 7, 10–12).

Recently, optimized proton MRI sequences for lung tissue have been reported (10) both for preclinical and clinical lung imaging. Briefly, these sequences are based on ultrashort echo time (UTE) and radial sampling of the *k*-space (10, 13). UTE proton MRI sequences have been demonstrated to be extremely efficient for limiting motion and susceptibility artifacts and for enhancing MRI signal intensity of the lung tissue (14–19).

At the same time in the last two decades, the design of new contrast agents has been actively pursued to improve the potential of MRI in early detection of pathologies. Multimodality, multivalency, combined therapeutic and imaging properties, or active targeting are indeed only some of the advantages that contrast media can provide (20–25).

In this work we implement and validate a noninvasive protocol which employs UTE MRI and multimodal contrast agents to

Significance

One of the main reasons for the dismal prognosis of lung cancer is related to late diagnosis of this pathology. In this work we show that the synergic employment of a properly chosen free-breathing MRI protocol and gadolinium-based nanoparticles allow early-stage accurate and noninvasive detection of millimetric-size lung tumor and of its contours. In addition, this work shows for the first time, to our knowledge, the advantages that can come from the choice of an orotracheal administration route instead of a more conventional systemic administration when studying pathomorphological changes due to lung cancers. Potential applications of this result may range from effective lung pathology detection and follow-up to pulmonary therapeutic applications of selected drugs.

Author contributions: A.B., J.-L.C., and Y.C. designed research; A.B., S.D., P.-Y.F., N.T., and Y.C. performed research; F.L. and O.T. contributed new reagents/analytic tools; A.B., S.D., P.-Y.F., and Y.C. analyzed data; and A.B., S.D., F.L., O.T., J.-L.C., and Y.C. wrote the paper.

The authors declare no conflict of interest.

This article is a PNAS Direct Submission.

[1]To whom correspondence should be addressed. E-mail: yannick.cremillieux@u-bordeaux2.fr.

This article contains supporting information online at www.pnas.org/lookup/suppl/doi:10.1073/pnas.1402196111/-/DCSupplemental.

detect in vivo lung parenchyma tumor pathological changes at submillimetric spatial resolution in an orthotopic mouse model of bioluminescent lung adenocarcinoma. The contrast agents, hereafter referred as ultrasmall rigid platforms (USRPs), were administered orotracheally to the animals. These nanoparticles are made of a polysiloxane matrix and are surrounded by gadolinium chelates covalently grafted to the inorganic matrix. A near-infrared fluorophore [cyanine (Cy) 5.5] is grafted onto some of the nanoparticles to permit fluorescence imaging. The hydrodynamic diameter of the nanoparticles is entirely under 5 nm and the mass around 8.5 kDa (24).

The sensitivity, specificity, contrast enhancement, and pharmacokinetics of this intrapulmonary [or intratracheal (i.t.)] administration route were evaluated against standard i.v. administration of contrast agents. The high-precision identification of tumor contours was validated with bioluminescence imaging (BLI) and conventional histological analysis. The accumulation of the USRPs in the tumor site was confirmed by 2D fluorescence reflectance imaging (FRI) exploiting the multimodal potential of these nanoassemblies.

Results

An orthotopic model of NSCLC morphologically similar to adenocarcinoma was developed in immunodeficient mice, inoculating luciferase-modified tumor cells into the lungs. The slow development of the tumor was monitored and quantified using BLI. After 30 d, all of the xenotransplanted animals developed a tumor and underwent MRI investigation for high-resolution detection of the lung tumor lesions. The signal intensity measured using BLI ranged from 5,168 photons per pixel per 30s to 28,935 photons per pixel per 30s, showing a significant heterogeneity in the development of the tumors.

Thirty-five days after inoculation, before the administration of contrast agent, free-breathing UTE MR images allowed identification of the presence of abnormal parenchymal tissue in a number of animals (~90%). Nonetheless, the contours of the carcinogenic formations were not easily identifiable (Fig. 1*A*). When detectable, the two independent observers agreed on the identification of the presence of the tumor in 93.2% of the examined slices.

After orotracheal or i.v. administration of USRPs, UTE MR images allowed the identification of the tumor in all the mice. For all of them, a good colocalization of the position of the tumor between MRI and BLI was observed (Fig. 1 *B–D*). Similarly, the approximate position of the tumor observed with UTE MRI was confirmed with histological analysis (Fig. 1*E*). All the observations by the two independent users on the localization of the tumors on MRI, BLI, and histology were highly concordant (98.5% of the cases).

The comparison of signal enhancement and increase of contrast-to-noise ratio (ΔCNR) in the identified tumors after the administration of the contrast agent (Fig. 2) showed approximately twofold higher values for the orotracheal (50 μL of 50 mmol/L [Gd^{3+}]) administration with respect to the i.v. one (200 μL of 50 mmol/L [Gd^{3+}]), using four times less Gd^{3+}. Moreover, the i.v. administration of a clinical commercially available contrast agent (Dotarem; Guerbet) was four times less effective than the same amount of i.v.-administered USRPs (200 μL of 50 mmol/L [Gd^{3+}]). This latter observation is related to the high rigidity of USRPs compared with commercially available contrast agents and the fact that USRPs carry about 10 ions of gadolinium each (r_1 per nanoparticle at 4.7 T ~82.2 $mM^{-1}{\cdot}s^{-1}$ vs. r_1 Dotarem at 4.7 T ~3 $mM^{-1}{\cdot}s^{-1}$). Typically, an increase in the average signal-to-noise ratio in lung tumor from 19.7 to 39.5, 30.9, and 24.3 was observed for the orotracheal administration of USRPs (50 μL of 50 mmol/L [Gd^{3+}]), i.v. administration of USRPs (200 μL of 50 mmol/L [Gd^{3+}]), and i.v. administration of Dotarem (200 μL of 50 mmol/L [Gd^{3+}]), respectively. Similarly, an average ΔCNR between tumor and healthy tissues from 7.2 to 20.4, 16.6, and 11.8 was observed for the orotracheal administration of USRPs (50 μL of 50 mmol/L [Gd^{3+}]), i.v. administration of USRPs (200 μL of 50 mmol/L [Gd^{3+}]), and i.v. administration of Dotarem (200 μL of 50 mmol/L [Gd^{3+}]), respectively. The coefficient of variation of the reference signal computed over all of the MRI measurements was <4%.

The accumulation of the nanoparticles in the tumor region was assessed and confirmed by 2D FRI in a subgroup of animals, exploiting the multimodal potential of the USRPs. Cy 5.5 dye was covalently grafted onto the nanoassemblies and FRI was performed before and after the i.v. or orotracheal administration of nanoparticles. Excellent colocalization was found between FRI, BLI, MRI, and histological analysis (Fig. S1). Due to the higher sensitivity of FRI compared with MRI, USRPs were visible in the tumor site up to 72 h after administration.

No signal enhancement was observed in tumor-bearing mice after i.v. or orotracheal administration of saline solution. Animals that were not inoculated with NSCLCs were used as controls. No signal enhancement was observed in their lungs after i.v. administration of contrast agent (Fig. S2), whereas homogeneous enhancements of their lung parenchyma were observed after orotracheal instillation (26, 27). The observed pharmacokinetics after orotracheal administration of contrast agents in the lungs of healthy animals reproduced the results observed in ref. 27, with fast diffusion of the nanoparticles in the lungs (average diffusion constant = 28 ± 12 min) and slow but uniform elimination from the parenchymal tissue (average elimination constant = 165 ± 31 min). In all animals a significant renal clearance and negligible hepatic elimination were observed, after orotracheal

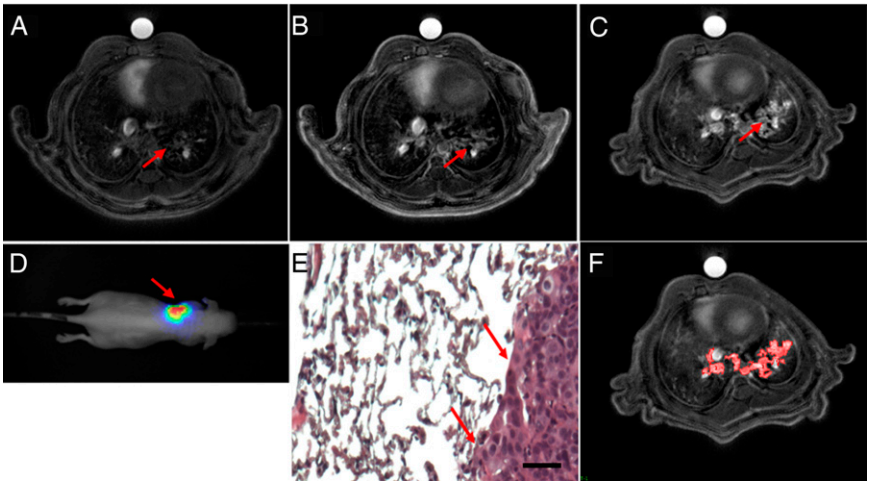

Fig. 1. UTE MRI axial slices of the tumor-bearing mice (*A*) before and (*B*) after the i.v. administration of 200 μL of 50mM [Gd^{3+}] USRP (day 35) or (*C*) the orotracheal administration of 50 μL of 50 mM [Gd^{3+}] USRP (day 38). The presence and colocalization of the tumor was assessed with (*D*) BLI and (*E*) histology. In *D* the scale colors are proportional to the number of detected photons per second. The arrows indicate the tumor in the left lung. In *E* an HES stain (100× magnification) from an axial slice approximately corresponding to the MR image plane is shown. (Scale bar: 50 μm.) (*F*) Image showing the typical segmentation procedure used to contour the tumor. The red area delineates the tumor segmented from *C*. Vessels were recognized because of their hyperintense signal and typical shape, and were thus excluded from the segmentation procedure.

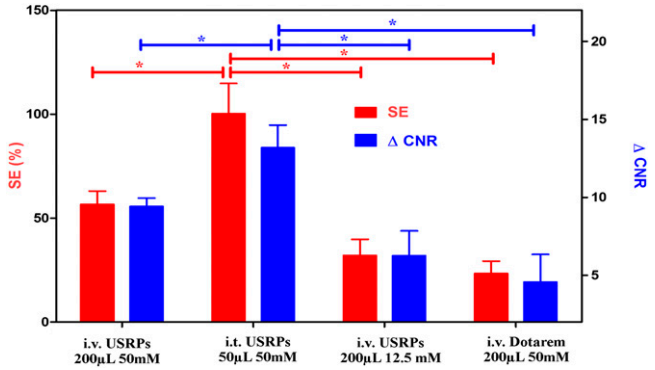

Fig. 2. Bar plot comparing the signal enhancement (red, left scale) and the ΔCNR (blue, right scale) for i.t. and i.v. administration of USRPs and Dotarem. Asterisks indicate significant differences ($P < 0.05$). Data are presented as mean value ± SEM.

or i.v. administration, as already reported in refs. 24, 26, and 27. This phenomenon is mostly related to the ultrasmall size of the nanoparticles (hydrodynamic diameter <5 nm) (24, 26–29).

In tumor-bearing mice, the pharmacokinetics observed in the tumor tissues after the i.v. administration of USRPs was sensibly different from the one observed after orotracheal administration, as shown in Fig. 3. Following i.v. administration, maximum signal enhancement of the tumor and CNR between tumor and healthy tissues were observed at the first acquired time point (10–20 min after injection). A rather fast elimination of the USRPs from the tumor tissue was then observed (50% drop of the signal enhancement observed in 62 ± 12 min).

On the other hand, maximum signal enhancement was observed between 50 and 110 min after the i.t. administration of USRPs. The elimination of the USRPs from the tumor after the orotracheal administration was about four times longer compared with i.v. injection (50% drop of the signal enhancement observed in 235 ± 56 min). The CNR curve presented the same behavior of the signal enhancement one, indicating that the optimal time points for tumor detection and segmentation are between 1 and 2 h after the orotracheal administration.

Tumors were contoured on the UTE MR images obtained after the administration of the contrast agent, using a previously validated semiautomatic segmentation procedure (Fig. 1*F*). The computed total tumor volume (average tumor volume 60.1 ± 5.4 mm^3, range 37.9–84.2 mm^3) was correlated with the bioluminescent signal to assess the precision of the segmentation protocol. The quantified tumor volumes significantly correlated with the measured bioluminescent signal both after i.t. ($R = 0.84$, $P < 0.01$) and i.v. ($R = 0.88$, $P < 0.01$) administration of USRPs (Fig. 4). Bland–Altman analysis showed an average bias of −1.8 mm^3 when the tumor was quantified after the i.v. injection compared with orotracheal administration.

A short-term reproducibility study for the orotracheal administration was performed. The subgroup of mice that received a second orotracheal administration of USRPs 3 d apart showed no significant differences in tumor size ($P > 0.24$), position,

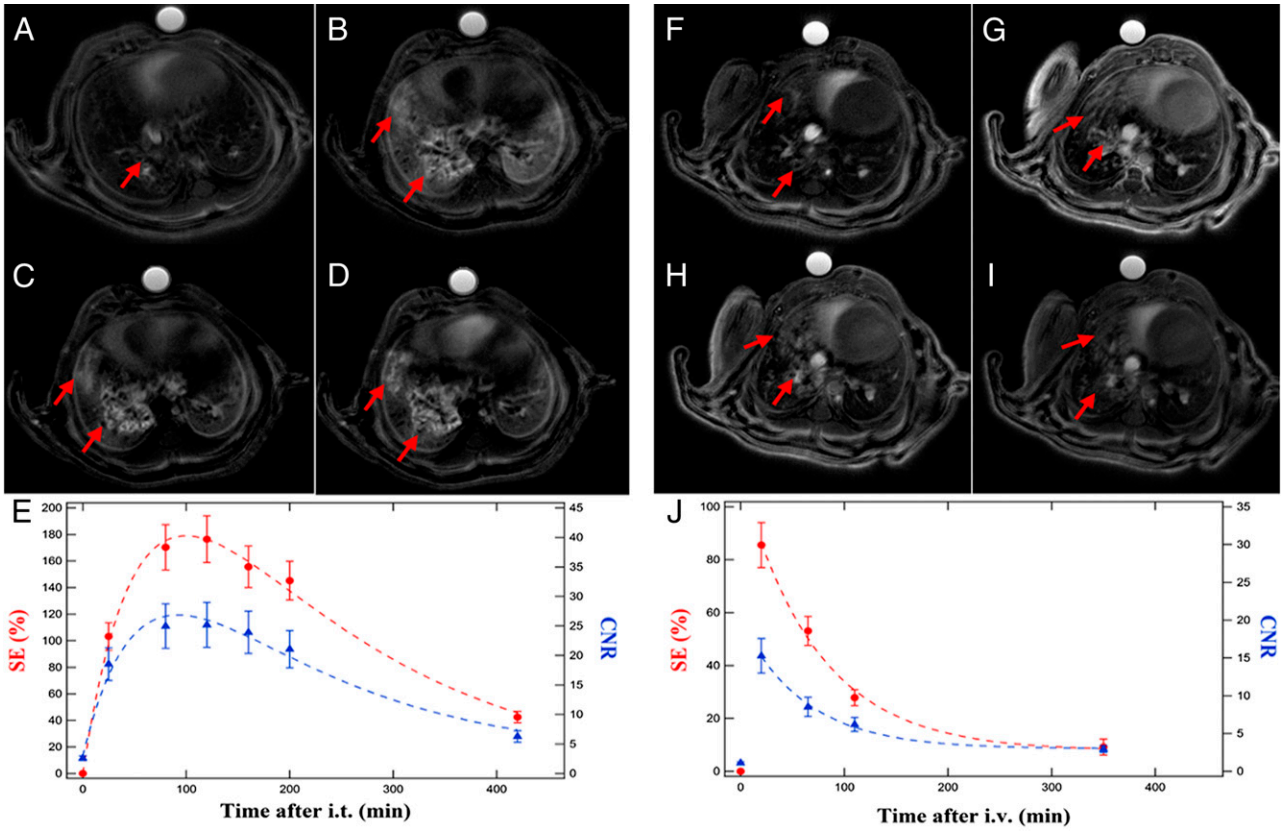

Fig. 3. Representative examples of UTE MRI axial slices showing USRP accumulation in the tumor in the function of time after (*A–E*) i.t. (50 μL of 50 mmol/L [Gd^{3+}], day 35) or (*F–J*) i.v. administration (200 μL of 50 mmol/L [Gd^{3+}], day 38). The curves of signal enhancement (red, left scale) and CNR (blue, right scale) in *E* and *J* show the sensibly different pharmacokinetics observed after the i.v. or i.t. route. Dashed lines are used to indicate the curves trend. *A* was acquired before the i.t. administration of USRPs; *B* is after 30 min, *C* after 100 min, and *D* after 180 min. *F* was acquired before the i.v. administration of USRPs; *G* is after 15 min, *H* after 60 min, and *I* after 110 min. The arrows indicate the presence of the tumor and the accumulation of USRPs in the neoplastic lesions. Data in *E* and *J* are presented as mean value ± SEM.

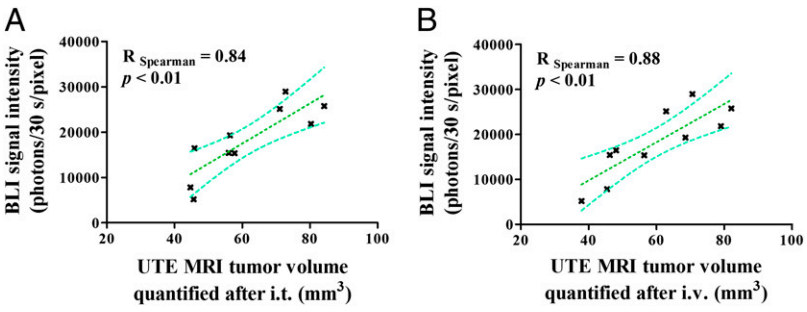

Fig. 4. Correlation plots between BLI signal intensity and quantified tumor volumes (*A*) after i.t. (day 38) or (*B*) i.v. administration (day 35). A significant correlation was found in both the cases; 95% confidence intervals are shown.

signal enhancement ($P > 0.68$), or ΔCNR ($P > 0.45$), confirming the reproducibility of the protocol (Fig. S3).

The possibility of studying the evolution of a tumor using the orotracheal administration protocol was evaluated. The subgroup of mice that received a second orotracheal administration of USRPs 16 d apart showed a significant increase in the tumor volume quantified with MRI ($P < 0.03$). Metastases in both lungs were observed in the majority of the animals at the second time point. No significant increase in the signal enhancement ($P > 0.25$) or ΔCNR ($P > 0.25$) was observed between the two time points (Fig. S4).

Discussion

The extravasation of small particles or molecules from abnormal tumor vessels and lack of lymphatic drainage in tumor tissues are generically referred to as the "enhanced permeability and retention" (EPR) effect (30, 31). These peculiar properties of tumor tissue are known to facilitate passive targeting and accumulation of diagnostic or therapeutic nanoparticles in tumors. As a matter of fact, tumor signal enhancement using gadolinium-based contrast agents is a common approach in clinical and preclinical MRI for improving the detection and the delineation of cancerous tissue (20, 23, 32). However, contrast enhancement of tumors located in the lung can be severely hampered by motion artifacts and unmatched magnetic susceptibility between air and tissues (6, 7, 10–12). In addition, for this organ, airway delivery of diagnostic or therapeutic compounds might be an efficient (yet unexplored) route for targeting lung tumors.

To address these lung-specific points, we investigated the possibility of implementing a noninvasive MRI protocol to be used in early in vivo detection and follow-up of NSCLCs. To do so, free-breathing UTE MRI was used in conjunction with orotracheal administration of ultrasmall gadolinium-based nanoparticles. Orotracheal administration for contrast agent delivery to lung tumor tissue was compared with standard i.v. injection with respect to signal and contrast enhancements and pharmacokinetics.

Both administration modalities allowed the computation of the tumor volumes that significantly correlated with the bioluminescent signal coming from the tumor cells. The precision of the described protocol was indeed confirmed by the significant linear correlation between MRI tumor volume quantification on UTE MR images and BLI measurements of orthotopic tumor growth. The excellent correlation of the number of photons emitted (proportional to the metabolically active tumor cells) (33, 34) and the MRI tumor volume measurements thus ensure the correctness and precision of the segmentation procedure (33, 34) achievable using UTE MR images in combination with USRPs. It has to be pointed out that, in this study, tumor volumes were not estimated using histological procedures. The absence of solid masses in the proposed NSCLC model may indeed complicate any histological tumor volume estimation. In addition, the fixation protocol required to identify the approximate position of the tumors may cause mechanical distortion of the extracted lungs (35), potentially introducing relevant sources of error in the histological tumor burden estimation. Lacking accurate validated ex vivo methods for diffuse lung tumor quantification, in vivo BLI signal intensity was by far the simplest and most effective choice to evaluate the precision of MRI measurements. The growing interest for these complementary noninvasive imaging techniques in preclinical lung imaging is strongly related to the possibility of combining the high-sensitivity of BLI with the good soft tissue contrast and high-resolution of MRI (36).

Significantly higher signal enhancements and CNRs were observed with orotracheal administration using lower doses. This finding is of crucial importance because, for the first time, to our knowledge, it demonstrates that higher performance of contrast agents can be obtained using an orotracheal administration route when targeting lung diseases. As a consequence, lower concentrations of contrast media can be used, reducing dose and potential safety issues (20, 37). In addition, lower interobserver variability in tumor segmentation might be reached thanks to the higher CNR and signal enhancement observed when an orotracheal route is chosen. Similarly, effective automatic segmentation procedures might be implemented, taking advantage of the high signal-to-noise ratios and CNRs in lung tumors after the orotracheal instillation of the contrast agents. These results support the growing interest in drug delivery via airways to target several diseases of the lung, but also of other organs (38). The bulk of the literature seems to indeed suggest that pulmonary administration is a practical, simple, efficient, and reliable route for lung and systemic delivery of drugs (39).

The surprising signal enhancement and CNR achievable after orotracheal administration cannot be entirely explained in the light of the EPR effect observed usually in tumor tissue following systemic administration of contrast agents. The suspected reason of the strong accumulation of nanoparticles in the tumor may be connected to the fact that, once in the alveoli, the USRPs can directly reach the tumor because no (or very compromised) alveolar barrier is interposed between the tumor and the contrast agent (Fig. 1*E*).

The pharmacokinetics observed after the two different administration modalities are significantly different. For i.v. administration, the maximum signal enhancement can be observed a few minutes after the administration of the contrast agent. Nanoparticles are then rapidly cleared from the lungs. This kind of pharmacokinetics presents the clear advantage of enabling a fast-imaging protocol which may translate into an effective patient management workflow in clinical practice.

On the contrary, after orotracheal administration, a roughly homogeneous signal enhancement can be observed in the lung parenchyma. Effective elimination of the contrast is then observed in the healthy lung tissue, whereas long retention is visible in the tumor tissues. This protocol presents the inconvenience related to the fact that the moment of highest contrast between tumor and healthy tissue has to be empirically determined to be effective. On the other hand, the high accumulation of nanoparticles (reflected in high signal enhancement and CNR) and the long residence times of the USRPs in the tumor permit to envisage several imaging and therapeutic protocols.

Ultrasmall gadolinium-based nanoparticles, similar to the ones presented in this work, have indeed been shown to have a potential theranostic application in brain tumors due to the radiosensitizing effect of the gadolinium atoms (40). The long retention of the USRPs in the tumor after orotracheal instillation

and the accurate knowledge of the pharmacokinetics of the contrast agent in healthy and diseased tissues would allow the tailoring of radiation therapy according to the accumulation effect measurable with MRI. As a consequence, this would optimize the theranostic efficacy of these nanoassemblies.

When measured only 3 d apart after orotracheal administration of USRPs, lung tumors were statistically identical (signal enhancement, ΔCNR, volume) and the position unchanged, confirming the reproducibility of the noninvasive measurements performed with the proposed method. In addition, as expected, when measured 2 wk apart, the nontreated carcinogenic formations increased in size and in tumor cell density. No increase in CNR or signal enhancement was observed, probably due to the fact that tumors internalized roughly the same amount of nanoparticles at the two different stages.

The accurate localization and delineation of tumors using both orotracheal and i.v. delivery of contrast agents was made possible with the use of appropriate UTE MRI sequences using radial *k*-space sampling, less sensitive to cardiorespiratory motion than Cartesian MR acquisitions (14–17). As a consequence, free-breathing acquisitions can be performed with limited impact on lung images signal-to-noise ratio, sharpness, and spatial resolution (16). This noninvasive free-breathing protocol is particularly interesting because it can be used in clinical studies with minimal changes. In this respect, the UTE MRI has been shown to be a promising sequence which can be applied in clinical studies of lung morphology, physiology, and pathologies (18, 19).

In conclusion, the observed high reproducibility and efficacy of the protocol, altogether, make the orotracheal administration of gadolinium-based nanoparticles a good candidate for early lung cancer detection and noninvasive follow-up of diseases. In addition, the previously demonstrated negligible acute toxicity of USRPs and favorable pharmacokinetics (26, 27), their theranostic properties (40), and the possibility of replacing orotracheal administration with a simpler aerosol, altogether, make the proposed protocol potentially translatable to human studies. To our knowledge this is the first time a study clearly shows that the synergic employment of a T_1-weighted UTE MRI sequence and gadolinium-based nanoparticles allow the detection of a millimetric-sized lung tumor and its contours. In addition, this work has shown, for the first time, also to our knowledge, the valuable advantages that can come from the choice of an orotracheal administration route instead of more conventional parenteral systemic administration when studying the pathomorphological changes due to NSCLCs. Potential application of this result may range from lung pathologies detection to pulmonary therapeutic applications of selected drugs or lead compounds.

Materials and Methods

Animals. Female Naval Medical Research Institute (NMRI) nude mice ($n = 20$; 5 wk-old) weighing 24.0 ± 0.5 g were purchased from Elevage Janvier (Le Genest). Before the beginning of the experiment, the animals were acclimatized in a temperature-controlled environment for 1 wk. Facility rooms were maintained at constant temperature (25 °C), humidity (30–50% relative humidity), and 12-h light:dark illumination cycle. Access to food and tap water was available ad libitum. Experiments were carried out following Institut National de la Santé et de la Recherche Médicale guidelines regarding the fair treatment of animals with approval of the Comité d'Éthique en Expérimentation Animale de Bordeaux.

Tumor Implantation. Luciferase-modified human NSCLC H358 cells (H358-Luc cells) were cultured in Roswell Park Memorial Institute medium, supplemented with 10% (vol/vol) heat-inactivated FBS. Before inoculation, they were harvested, washed, and resuspended in PBS 1× (10^7 cells per 50 μL). Thirty days before the beginning of the imaging protocol, animals ($n = 16$) were anesthetized using an i.p. injection of 0.1 μg/g medetomidin (Axience) and 0.1 mg/g ketamine (Panpharma), and tumor cells inoculated in the lungs with a catheter after orotracheal intubation (performed with a 22-gauge Teflon i.v. catheter). Animals were left in the temperature- and humidity-controlled environment described above for 30 d. Four mice did not undergo the orthotopic implantation and were left as controls ($n = 4$).

Nanoparticle Synthesis and Characterization. The gadolinium-tetraazacyclododecanetetraacetic acid-based nanoparticles were synthesized and characterized according to the previously described protocol (27). To perform FRI, Cy 5.5 near-infrared dye was covalently grafted onto the nanoparticles (27). Further details about the characterization can be found in *SI Nanoparticle Characterization*.

Imaging Protocol. On day 30, animals were imaged using BLI to monitor the development of lung tumors. MR images were acquired starting from day 35. A capillary containing a gadolinium-based contrast agent was used as a reference in all of the MRI acquisitions. Between two different administrations of contrast agent on the same mouse, at least 2 d without any handling was foreseen to allow for complete elimination of the previously administered contrast agents (26, 27). After the last imaging point, animals were killed for histological analysis.

i.v. and orotracheal administration for tumor localization and pharmacokinetics study. All animals (including the $n = 4$ controls) were imaged with MRI at day 35 before and after receiving an i.v. administration of 200 μL of 50 mmol/L [Gd^{3+}] USRP. MRI was performed on day 38 before and after an orotracheal administration of 50 μL of 50 mmol/L [Gd^{3+}] USRP.

The orotracheal administration was performed according to the same protocol described in ref. 41, changing only the anesthesia modality. Briefly, mice were anesthetized using 4% isoflurane in a mixture of N_2:O_2 (80:20) via facial mask and, for the nebulization of contrast agent into the lungs, an IA-1C Microsprayer (Penn-Century, Inc.) connected to an FMJ-250 high-pressure syringe (Penn-Century, Inc.) was inserted into the trachea passing through the oral cavity.

A subgroup ($n = 4$) of tumor-bearing mice was imaged with MRI at day 41 after i.v. administration of 200 μL of 12.5 mmol/L [Gd^{3+}] USRP and at day 44 after i.v. administration of 200 μL of 50 mmol/L [Gd^{3+}] commercial gadoteric acid contrast agent (Dotarem). A subgroup ($n = 2$) of tumor-bearing mice were imaged with MRI at day 41 after orotracheal administration of a 50-μL solution of NaCl 0.9% and at day 44 after i.v. administration of 200 μL of NaCl 0.9%.

FRI. A subgroup ($n = 3$) of tumor-bearing mice were imaged with FRI at day 41 after i.v. administration of 200 μL of 50 mmol/L [Gd^{3+}] USRP and a subgroup ($n = 3$) of tumor-bearing mice were imaged with FRI at day 41 after orotracheal administration of 50 μL of 50 mmol/L [Gd^{3+}] USRP. Different animals were used for the two studies because of the long-lasting fluorescence signal.

Reproducibility of cancer detection through orotracheal administration. A subgroup ($n = 4$) of tumor-bearing mice received a second orotracheal administration of 50 μL of 50 mmol/L [Gd^{3+}] USRP at day 41 before and after being imaged with MRI to study the reproducibility of the tumor detection after i.t. administration.

Longitudinal monitoring of lung cancer. A subgroup ($n = 4$) of tumor-bearing mice received a second orotracheal administration of 50 μL of 50 mmol/L [Gd^{3+}] USRP at day 54 before and after being imaged with MRI to study the evolution of the tumor (follow-up study). These mice were imaged a second time using BLI on day 55 and killed for lung extraction immediately after.

Histology. Right and left lungs were dissected out, fixed with 4% paraformaldehyde (prepared in PBS, pH 7.2) in inflation using i.t. injection, and embedded in paraffin. Every 50 μm, two 4-μm-thick slices were cut and enumerated to approximately preserve the spatial information. On average, 100 slices were cut for each mouse. Slices were stained with hematoxylin–eosin–saffron (HES) to assess the general morphology and evaluated to verify the presence of the tumor and its approximate spatial location.

MRI. The images were acquired with a 4.7-T Biospec 47/50 spectrometer (Bruker), using a transmitter/receiver quadrature coil of 25 mm inner diameter (Bruker) and high-performance gradients (6-cm inner diameter, 1,000 mT/m, 100-μs ramp time). Mice were placed prone in a custom-built plastic holder and kept anesthetized with 2.5% isoflurane in a mixture of N_2:O_2 (80:20) via facial mask. Body temperature was kept constant using warm circulating water and the respiratory cycle was monitored constantly using a pressure sensor placed on the abdomen. The images were acquired with a UTE sequence, according to the MRI acquisition protocol described in ref. 26, increasing the repetition time to 210 ms (total acquisition time of about 11 min). Images were reconstructed with in-house software implemented in Interactive Data Language (Research Systems, Inc.), as described in ref. 27. All of the images were saved and analyzed with freeware medical image analysis software [Medical Image Processing, Analysis, and Visualization (MIPAV, http://mipav.cit.nih.gov), National Institutes of Health, Bethesda].

Image Analysis. The presence and position of the tumor in MR images was assessed by two independent users for all of the mice, according to a blinded procedure relative to animal implantation. When the tumor was identified in MR images, the tumor position in BLI and histological images was verified by the two independent observers. For each MR image, tumors were identified and regions of interest (ROIs) in the tumor and in the healthy parenchyma were manually segmented to measure the total average signal. The noise of the images was quantified as the SD of the mean signal of an ROI selected in the image background and the signal-to-noise in the tumor was computed. The CNR in each image was computed as the difference between the signal in the tumor and in the healthy tissue, normalized to the SD of the image noise. The ΔCNR was computed as the difference between the CNR before and after the administration of the contrast agent.

The volume of the tumor in the lungs was quantified with a semiautomatic segmentation procedure. In particular, a low-intensity threshold was applied to the images to exclude healthy parenchyma regions of the lung. The lung tumor was contoured with a semiautomatic tool able to generate contours while moving over the different structures of the lung, recognizing the level of intensity of each pixel and selecting regions according to the default preset parameters (MIPAV, active-contour algorithm LevelSet). The total tumor volume was computed multiplying the slice thickness by the sum of all of the areas segmented in the 10 consecutive slices, according to a protocol readapted from refs. 17 and 42. Main vessels were recognized thanks to their extremely high-intensity signal and typical shapes, and excluded from the segmentation contours.

The pharmacokinetics of the USRP contrast agent in the tumor region was studied according to the protocol already described in ref. 27.

BLI. Five minutes after i.p. injection of 150 μg/g luciferin (Promega), the mice were anesthetized and bioluminescence images and black-and-white pictures were acquired using a back-thinned CCD camera at −80 °C (ORCAII-BT-512G; Hamamatsu), as previously described (27). The intensity of tumor BLI signal (approximately proportional to the number of tumor cells) was measured and correlated to the tumor volume measured with MRI after i.v. or i.t. administration (34).

FRI. FRI was performed using the protocol described in ref. 27.

Statistical Analysis. Comparison of CNR, signal enhancement, and tumor volumes at different time points was performed using the Friedman nonparametric test with Dunn's multiple comparison (nonparametric equivalent of the repeated measures ANOVA test). Correlation between BLI signal intensities and MRI tumor volumes was performed using Spearman's correlation test. A Bland–Altman analysis was performed to evaluate possible biases between the two quantifications. Significance was fixed at a 5% probability level. All analyses were performed using GraphPad Prism (GraphPad Software Inc.). All of the data are presented as mean value ± SEM.

ACKNOWLEDGMENTS. The authors thank Dr. Sylvain Miraux for providing the mouse RF coil and Dr. Nathalie Senant for help in histological analysis. A.B. acknowledges a fellowship from the Pulmonary Imaging Network (PINET), FP7-PEOPLE-2010-ITN-264864. The authors acknowledge the support of the Agence Nationale de la Recherche (ANR) (ANR-12-P2N-0009) for the ANR Project Gd-Lung.

1. Parkin M, et al. (2004) Lung cancer epidemiology and etiology. *Pathology and Genetics of Tumours of the Lung, Pleura, Thymus and Heart*, eds Travis WD, Brambilla E, Müller-Hermelink HK, Harris CC (WHO Press, Geneva), pp 12–15.
2. Ferlay J, et al. (2013) GLOBOCAN 2012 Version 1.0, Cancer Incidence and Mortality Worldwide: IARC CancerBase No. 11. (International Agency for Research on Cancer, Lyon, France). Available at http://globocan.iarc.fr. Accessed January 1, 2014.
3. Molina JR, Yang P, Cassivi SD, Schild SE, Adjei AA (2008) Non-small cell lung cancer: Epidemiology, risk factors, treatment, and survivorship. *Mayo Clin Proc* 83(5):584–594.
4. Travis WD, Brambilla E, Müller-Hermelink HK, Harris CC (2004) *Pathology and Genetics of Tumours of the Lung, Pleura, Thymus and Heart* (WHO Press, Geneva).
5. Herbst RS, Heymach JV, Lippman SM (2008) Lung cancer. *N Engl J Med* 359(13): 1367–1380.
6. Lipson DA, Van Beek EJR (2005) *Functional Lung Imaging* (Taylor & Francis Group, Boca Raton, FL).
7. Biederer J, et al. (2012) MRI of the lung (2/3). Why . . . when . . . how? *Insights Imaging* 3(4):355–371.
8. Brenner DJ, Hall EJ (2007) Computed tomography—an increasing source of radiation exposure. *N Engl J Med* 357(22):2277–2284.
9. Edelman RR, Hesselink JR, Zlatkin MB, Crues JV, III (2006) *Clinical Magnetic Resonance Imaging* (Saunders-Elsevier, Philadelphia).
10. Wild JM, et al. (2012) MRI of the lung (1/3): Methods. *Insights Imaging* 3(4):345–353.
11. Beckmann N, et al. (2007) Lung MRI for experimental drug research. *Eur J Radiol* 64(3):381–396.
12. Wielpütz M, Kauczor H-U (2012) MRI of the lung: State of the art. *Diagn Interv Radiol* 18(4):344–353.
13. Bernstein MA, King KF, Zhou XJ (2004) *Handbook of MRI Pulse Sequences* (Elsevier, Burlington, MA).
14. Bergin CJ, Pauly JM, Macovski A (1991) Lung parenchyma: Projection reconstruction MR imaging. *Radiology* 179(3):777–781.
15. Bergin CJ, Noll DC, Pauly JM, Glover GH, Macovski A (1992) MR imaging of lung parenchyma: A solution to susceptibility. *Radiology* 183(3):673–676.
16. Zurek M, Bessaad A, Cieslar K, Crémillieux Y (2010) Validation of simple and robust protocols for high-resolution lung proton MRI in mice. *Magn Reson Med* 64(2): 401–407.
17. Bianchi A, Ozier A, Ousova O, Raffard G, Crémillieux Y (2013) Ultrashort-TE MRI longitudinal study and characterization of a chronic model of asthma in mice: Inflammation and bronchial remodeling assessment. *NMR Biomed* 26(11):1451–1459.
18. Johnson KM, Fain SB, Schiebler ML, Nagle S (2013) Optimized 3D ultrashort echo time pulmonary MRI. *Magn Reson Med* 70(5):1241–1250.
19. Lederlin M, Crémillieux Y (2013) Three-dimensional assessment of lung tissue density using a clinical ultrashort echo time at 3 tesla: A feasibility study in healthy subjects. *J Magn Reson Imaging*, 10.1002/jmri.24429.
20. Merbach AE, Toth E (2001) *The Chemistry of Contrast Agents in Medical Magnetic Resonance Imaging* (John Wiley & Sons, New York).
21. van Echteld CJA, Beckmann N (2011) A view on imaging in drug research and development for respiratory diseases. *J Pharmacol Exp Ther* 337(2):335–349.
22. Weissleder R, Pittet MJ (2008) Imaging in the era of molecular oncology. *Nature* 452(7187):580–589.
23. Ferrari M (2005) Cancer nanotechnology: Opportunities and challenges. *Nat Rev Cancer* 5(3):161–171.
24. Lux F, et al. (2011) Ultrasmall rigid particles as multimodal probes for medical applications. *Angew Chem Int Ed Engl* 50(51):12299–12303.
25. Mignot A, et al. (2013) A top-down synthesis route to ultrasmall multifunctional Gd-based silica nanoparticles for theranostic applications. *Chemistry* 19(19):6122–6136.
26. Bianchi A, Lux F, Tillement O, Crémillieux Y (2013) Contrast enhanced lung MRI in mice using ultra-short echo time radial imaging and intratracheally administrated Gd-DOTA-based nanoparticles. *Magn Reson Med* 70(5):1419–1426.
27. Bianchi A, et al. (2013) Quantitative biodistribution and pharmacokinetics of theranostic multimodal gadolinium-based nanoparticles for lungs using Ultrashort-TE MRI. *Magn Reson Mater Phy*, 10.1007/s10334-013-0412-5.
28. Choi HS, et al. (2010) Rapid translocation of nanoparticles from the lung airspaces to the body. *Nat Biotechnol* 28(12):1300–1303.
29. Choi HS, et al. (2010) Design considerations for tumour-targeted nanoparticles. *Nat Nanotechnol* 5(1):42–47.
30. Maeda H, Wu J, Sawa T, Matsumura Y, Hori K (2000) Tumor vascular permeability and the EPR effect in macromolecular therapeutics: A review. *J Control Release* 65(1-2): 271–284.
31. Matsumura Y, Maeda H (1986) A new concept for macromolecular therapeutics in cancer chemotherapy: Mechanism of tumoritropic accumulation of proteins and the antitumor agent smancs. *Cancer Res* 46(12 Pt 1):6387–6392.
32. Cheng W, Ping Y, Zhang Y, Chuang KH, Liu Y (2013) Magnetic resonance imaging (MRI) contrast agents for tumor diagnosis. *J Healthc Eng* 4(1):23–45.
33. Söling A, Rainov NG (2003) Bioluminescence imaging in vivo - application to cancer research. *Expert Opin Biol Ther* 3(7):1163–1172.
34. Rehemtulla A, et al. (2000) Rapid and quantitative assessment of cancer treatment response using *in vivo* bioluminescence imaging. *Neoplasia* 2(6):491–495.
35. Hsia CC, Hyde DM, Ochs M, Weibel ER; ATS/ERS Joint Task Force on Quantitative Assessment of Lung Structure (2010) An official research policy statement of the American Thoracic Society/European Respiratory Society: Standards for quantitative assessment of lung structure. *Am J Respir Crit Care Med* 181(4):394–418.
36. Im GH, et al. (2014) Improvement of orthotopic lung cancer mouse model via thoracotomy and orotracheal intubation enabling in vivo imaging studies. *Lab Anim* 48(2):124–131.
37. Runge VM (2002) Contrast media. *Clinical MRI*, ed Runge VM (WB Saunders, Philadelphia), pp 454–472.
38. Patton JS, Fishburn CS, Weers JG (2004) The lungs as a portal of entry for systemic drug delivery. *Proc Am Thorac Soc* 1(4):338–344.
39. Patton JS, Byron PR (2007) Inhaling medicines: Delivering drugs to the body through the lungs. *Nat Rev Drug Discov* 6(1):67–74.
40. Le Duc G, et al. (2011) Toward an image-guided microbeam radiation therapy using gadolinium-based nanoparticles. *ACS Nano* 5(12):9566–9574.
41. Gagnadoux F, et al. (2005) Aerosol delivery of chemotherapy in an orthotopic model of lung cancer. *Eur Respir J* 26(4):657–661.
42. Beckmann N, et al. (2001) Pulmonary edema induced by allergen challenge in the rat: Noninvasive assessment by magnetic resonance imaging. *Magn Reson Med* 45(1): 88–95.